Seismic imaging with optimal source wavefield reconstruction

Ivan Lim Chen Ning & Paul Sava, Center for Wave Phenomena, Colorado School of Mines

SUMMARY

Reverse time migration (RTM) is commonly regarded as a memory intensive operation because of the need to access source and receiver wavefields synchronously, which in principle require a large amount of storage. Many methods are proposed to manipulate the source wavefield efficiently, such as storing the wavefield in several layers around the computational domain for reconstruction. By using the integral solution of the representation theorem, we can reduce the boundary storage to a single layer without compromising accuracy. We propose such reconstruction of the source wavefield for elastic imaging to reduce the memory and the computational costs. Numerical RTM examples show that our proposed wavefield reconstruction method using a single boundary layer is comparable to the full storage of the source wavefield. We verify our method for elastic RTM and LSRTM on a distributed acoustic sensing (DAS) vertical seismic profile (VSP) dataset from the Eagle Ford shale formation.

INTRODUCTION

RTM exploits the correlation between the source and receiver wavefields at all times and positions. A naive implementation of RTM would compute and store both source and receiver wavefields before correlation. However, accessing large 4D (space and time) hypercubes is expensive, both for storage and disk I/O. Since the RTM imaging condition implies zero-lag crosscorrelation, we construct the image gradually over time while accessing the reconstructed wavefields to alleviate the storage burden which requires wavefields to be readily available for simultaneous access. However, methods have been reported in the literature to efficiently store parts of the source wavefield and reconstruct on the fly along with the receiver wavefield. This approach reduces the I/O load significantly by a slight increase in computation cost.

A way to tackle the storage and I/O problem is through optimal checkpointing by saving intermediate time snapshots of the source wavefield and recursively filling in the wavefield at other times when necessary for correlation with the receiver wavefield (Symes, 2007; Anderson et al., 2012). Further memory and computational reduction can be achieved by storing the wavefield around the domain at a conventional boundary (Dussaud et al., 2008; Nguyen and McMechan, 2014; Yang et al., 2014) or at a random boundary (Clapp, 2009; Shen and Clapp, 2011, 2015; Jia and Yang, 2017). Reconstruction from random boundaries causes artifacts in the wavefield due to scattering from the perturbations in the boundary zone. Alternatively, storing at least half the finite-difference stencil size allows more accurate wavefield reconstruction. Further storage reduction is achievable by saving intermediate time steps, followed by filling the wavefield through interpolation (Yang et al., 2016). However, increasing finite-difference accuracy expands the boundary layer storage requirement for accurate reconstruction. Saving a linear combination of the wavefields (Liu et al., 2015) or gradually reducing the finite-difference order while approaching the boundaries (Bo and Huazhong, 2011) decreases the memory requirement at the expense of reconstruction accuracy. A different approach while maintaining accuracy is through the Lax-Wendroff method by obtaining spatial derivative from temporal derivatives on the boundary (Tan and Huang, 2014; Mulder, 2017).

Accurate wavefield reconstruction from a single boundary layer around the computational domain is possible using the representation theorem via multiple point sources approach (Morse and Feshbach, 1953; Masson et al., 2013), which is demonstrated by Vasmel and Robertsson (2016) in acoustic media. Ravasi and Curtis (2013) exploit the representation theorem for elastic wavefield extrapolation that avoids nonphysical waves (wave modes reconstructed during reverse-time extrapolation that were not present in the observed data). We propose to use the representation theorem for accurate reconstruction of the elastic source wavefield from data stored on a single boundary layer. Raknes and Weibull (2016) demonstrate a similar approach using an approximation of the representation theorem, which leads to nonphysical wave modes in the reconstructed wavefield. In this paper, we honor the full representation theorem for wavefield reconstruction and illustrate the feasibility of the method with numerical examples of elastic RTM.

METHODOLOGY

We describe elastic-wave propagation using the second-order partial differential equations in space $\mathbf{x}$ and time t consisting both stress tensor $\underline{\mathbf{t}}(\mathbf{x},t)$ and the particle displacement vector $\mathbf{u}(\mathbf{x},t)$ wavefields (Aki and Richards, 2002)

$$\rho\,\frac{\partial^2\mathbf{u}}{\partial t^2} = \nabla\cdot\underline{\mathbf{t}}+\mathbf{f}, \tag{1}$$

where $\rho(\mathbf{x})$ is the density and $\mathbf{f}(\mathbf{x},t)$ is an external volume force. The stress and strain $\underline{\mathbf{e}}(\mathbf{x},t)$ tensors are related through the constitutive relation with the assumption of linear elasticity

$$\underline{\mathbf{t}} = \underline{\underline{\mathbf{c}}}\,(\underline{\mathbf{e}}+\underline{\mathbf{h}})\,, \tag{2}$$

where $\underline{\mathbf{h}}(\mathbf{x},t)$ is the external deformation source which together with the stiffness tensor $\underline{\underline{\mathbf{c}}}(\mathbf{x})$ forms a stress perturbation source $\underline{\mathbf{m}}(\mathbf{x},t) = \underline{\underline{\mathbf{c}}}(\mathbf{x})\,\underline{\mathbf{h}}(\mathbf{x},t)$. The relationship between the strain tensor and the particle displacement is

$$\underline{\mathbf{e}} = \frac{1}{2}\left\{\nabla\mathbf{u}+(\nabla\mathbf{u})^{\mathsf{T}}\right\}. \tag{3}$$

The representation theorem describing the particle motion in a volume Ω due to a body force $\mathbf{f}$ together with the traction $\underline{\mathbf{t}}\cdot\mathbf{n}$ and the displacement on the surface $\partial\Omega$ is given in the convolution form as (Aki and Richards, 2002)

$$\begin{aligned}\mathbf{u}(\mathbf{x}) = &\iiint_{\Omega} dV\,\mathbf{f}(\boldsymbol{\xi})*\mathbf{G}(\mathbf{x},\boldsymbol{\xi})+\\ &\oiint_{\partial\Omega} ds\left[\underline{\mathbf{t}}(\boldsymbol{\xi})*\mathbf{G}(\mathbf{x},\boldsymbol{\xi})-\underline{\underline{\mathbf{c}}}\,\mathbf{u}(\boldsymbol{\xi})*\frac{\partial\mathbf{G}(\mathbf{x},\boldsymbol{\xi})}{\partial\boldsymbol{\xi}}\right]\cdot\mathbf{n},\end{aligned} \tag{4}$$

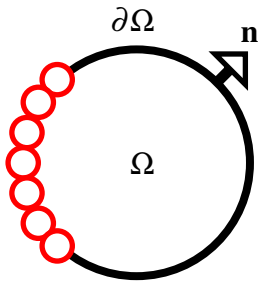

Figure 1: Schematic diagram illustrating the elements of the representation theorem. The black circle denotes the surface $\partial\Omega$ enclosing a volume Ω with the corresponding normal vector $\mathbf{n}$ pointing outwards. The red circles denote some sources/receivers locations.

where $*$ denotes time convolution. $\boldsymbol{\xi}$ and $\mathbf{x}$ are the source and evaluation locations, respectively. The vector $\mathbf{n}$ is normal to the closed surface $\partial\Omega$ surrounding the volume Ω. Figure 1 illustrates the physical elements of the representation theorem. Assuming that no external volume forces $\mathbf{f}$ are present, the volume integral disappears. The surface integral vanishes if we assume a homogeneous boundary condition (Gangi, 1970). When the traction $\underline{\mathbf{t}}\cdot\mathbf{n}$ and the displacement $\mathbf{u}$ on the surface $\partial\Omega$ enclosing the volume Ω are excited from the external volume force $\mathbf{f}$ within the volume, i.e. the data recorded on a surface, we can express the particle displacement $\mathbf{v}$ wavefield inside the volume Ω surrounded by the surface $\partial\Omega$ as

$$\mathbf{v}(\mathbf{x}) = -\oiint_{\partial\Omega} ds \left[\underline{\mathbf{t}}(\boldsymbol{\xi}) * \mathbf{G}(\mathbf{x},\boldsymbol{\xi}) - \underline{\underline{\mathbf{c}}}\,\mathbf{u}(\boldsymbol{\xi}) * \frac{\partial \mathbf{G}(\mathbf{x},\boldsymbol{\xi})}{\partial \boldsymbol{\xi}}\right]\cdot\mathbf{n}. \tag{5}$$

The Green's function $\mathbf{G}(\mathbf{x},\boldsymbol{\xi})$ in equation 5 denotes a wave-propagator using the external volume force $\mathbf{f}$ as source. The stiffness tensor $\underline{\underline{\mathbf{c}}}$ together with the spatial derivative of the Green's function $\partial\mathbf{G}(\mathbf{x},\boldsymbol{\xi})/\partial\boldsymbol{\xi}$ form the equivalent of a wave-propagator using an external deformation force $\underline{\mathbf{h}}$ as source. The sign inside the integral changes to negative to denote backward propagating Green's function (Wapenaar, 2014).

To obtain the integral solution of the representation theorem, we use the multiple point sources method (Morse and Feshbach, 1953; Masson et al., 2013) to turn the saved wavefield along the boundary $\partial\Omega$ into sources. In order to reconstruct the source wavefield using the representation theorem, we save the source wavefield along the boundary $\partial\Omega$ (black dots), as highlighted in the left panel of Figure 2, which requires less memory than conventional methods storing at least half (Yang et al., 2014) of the finite-difference stencil size on the boundary, as shown in the right panel of Figure 2.

Our goal is to perform elastic RTM and least-squares RTM (LSRTM) by reconstructing the source wavefield on the fly. To avoid comparing multiple elastic RTM images for a given experiment, we adopt the energy imaging condition (Rocha et al., 2017) which generates a single elastic image without

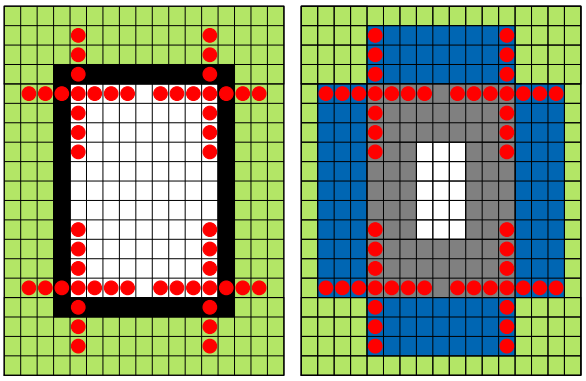

Figure 2: Illustration of the computational (in white) and boundary domains (in green). The left panel shows a single boundary layer (black dots) while the right panel illustrates conventional approach that requires storage of half the finite-difference stencil either in the computational (in gray) or in the boundary (in blue) domains.

wave-mode decomposition. We modify the potential term of the imaging condition to exploit the forward simulated displacement and stress wavefields $(\mathbf{u},\underline{\mathbf{t}})$ together with the adjoint displacement and strain wavefields $\left(\mathbf{u}^{\dagger},\underline{\mathbf{e}}^{\dagger}\right)$

$$\mathcal{I}(\mathbf{x}) = \sum_{t}\left(\rho\dot{\mathbf{u}}\cdot\dot{\mathbf{u}}^{\dagger} - \underline{\mathbf{t}}\cdot\underline{\mathbf{e}}^{\dagger}\right), \tag{6}$$

where $\mathcal{I}(\mathbf{x})$ is the elastic energy image. The dot $(\dot{})$ represents time derivative, and the dagger $(^{\dagger})$ denotes adjoint. The reformulation allows us to avoid re-computation of wavefield derivatives in the kinetic term of the imaging condition as we solve equation 1 through the elastodynamics relation.

NUMERICAL EXAMPLE

Figure 3 shows the acquisition geometry for our synthetic experiment and the P-wave velocity. The S-wave velocity and density are constant at 1.5 km and 1 g/cm^3, respectively. We save the forward extrapolated source wavefield to serve as a reference for the wavefield reconstructed from the single layer boundary. We perform elastic RTM using the energy norm

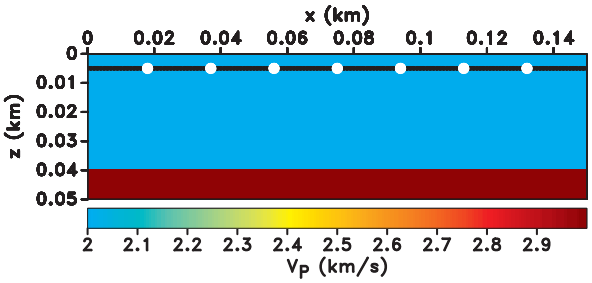

Figure 3: (a) The P-wave velocity model with an overlay of a 2D experiment depicting the source (white dots) and receiver (black line) locations.

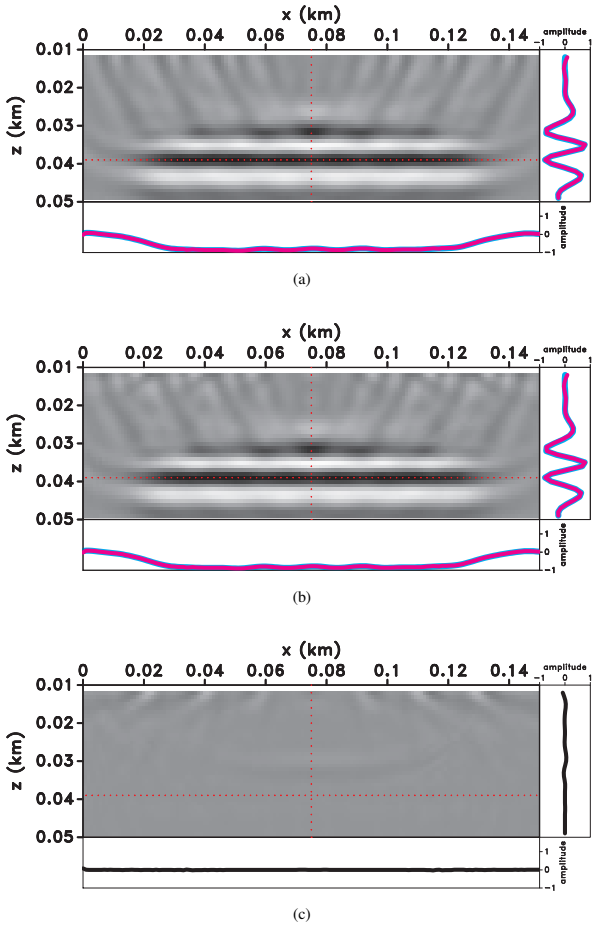

Figure 4: Energy norm elastic RTM for 7 shots using (a) reference and (b) reconstructed source wavefields. (c) The corresponding difference between (a) and (b). The graphs on the left and bottom are profile along the reflection and the middle of the image, respectively as indicated by the red dotted lines. The amplitude profiles correspond to (a) blue, (b) red, and (c) black.

imaging condition with all 7 shots. The reference wavefield produces the reference image shown in Figure 4b, while Figure 4a depicts the image using the reconstructed source wavefields. Figure 4c shows the amplitude difference at the source location due to the source wavefield expanding beyond wavelet peak time and the four corners of the computational domain where the normal vectors **n** are undefined generating reconstruction artifacts. The semi-vertical events at 0.01, 0.03, 0.05, 0.06, 0.07, 0.10, 0.12, and 0.14 km are crosstalk between the source and receiver wavefields that propagate along the horizontal axis. Amplitude profiles for the reference (in blue) and reconstructed source wavefield (in red) images along the depth direction (vertical dotted line) in the middle and along the horizontal direction (horizontal dotted line) at the reflection depth are in excellent agreement overall. The residual sum of squares (RSS) for the difference image normalized to the reference image is approximately 1%.

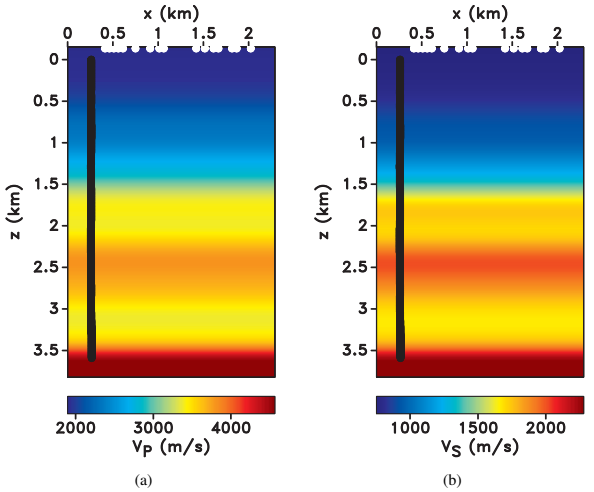

Figure 5: Panel (a) shows the P-wave velocity obtained through first-break picking, while panel (b) shows the S-wave velocity obtained from the well logs. Both panels show the acquisition geometry with the receivers in black and sources in white.

FIELD DATA EXAMPLE

We also validate our method using a 2D distributed acoustic sensing (DAS) vertical seismic profile (VSP) dataset from Lavaca County Texas, USA. The data comprise of two sections in the deviated well but we use the vertical portion due to poor signal-to-noise ratio and the directivity of DAS measurement in the horizontal section. The sample spacing of the DAS data is approximately 8 m with gauge length of 10 m. Figure 5a shows the compressional velocity obtained through first-break picking and Figure 5b shows the shear velocity derived from well logs. We image the upgoing wavefield from the VSP data with the energy norm imaging condition.

RTM images for the 16 shots are depicted in Figures 6a and 6b for the reference and reconstructed source wavefield, respectively. We apply a poststack amplitude gain with one power of depth to balance the shallow and deep events. The corresponding amplitude difference in Figure 6c is minimal due to the power of stack across multiple shots with the RSS normalized to the reference image of approximately 0.01%. We remove the migration smiles before stacking by dip filtering for better interpretability, as shown in Figures 6d and 6e. The low amplitude differences in Figure 6f are the same as in Figure 6c where the RSS normalized to the reference image is approximately 0.005%.

Figures 7a and 7b show the LSRTM images for all shots after dip filtering and poststack amplitude gain using the reference and the reconstructed source wavefield, respectively. The images are indistinguishable through visual inspection. However, the slight amplitude difference as shown in Figure 7c is the result of stacking coherent differences between the shots with an increase of the RSS normalized to the reference image to 2%. The amplitude differences result from propagating the artifact

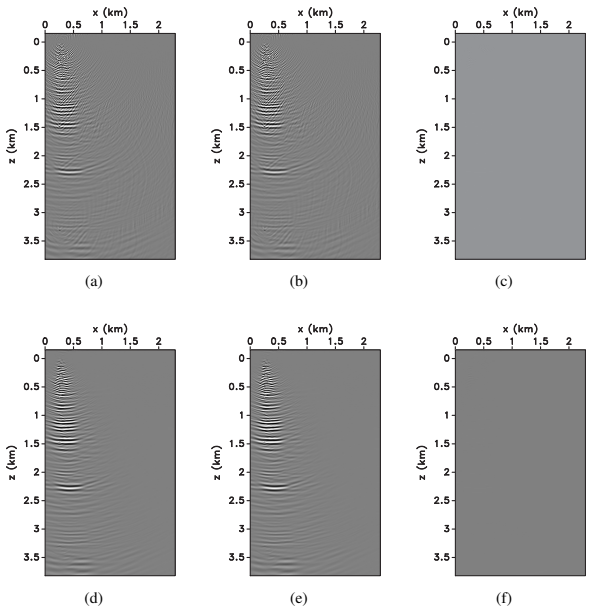

Figure 6: RTM image using (a) reference and (b) reconstructed source wavefield. (c) The difference between (a) and (b) panels. (d)-(e) show images equivalent to (a)-(c) after dip filtering and poststack amplitude gain.

located around the source during the least-squares process.

The initial data residual for LSRTM using the reference and reconstructed source wavefields are shown in Figures 8a and 8b, respectively. The final residuals are shown in Figures 8c and 8d, and indicate that the least-squares process matches the majority of data arrivals. The more prominent residual for the bottom two reflectors around 2.25 and 3.5 km in depth is due to the weaker amplitude of the modeled DAS response, as shown in Figures 8e and 8f.

CONCLUSIONS

We produce accurate elastic RTM and LSRTM images of the subsurface with source wavefields reconstructed synchronously with the receiver wavefields from information stored in a single layer boundary. Reducing the dimension of the stored source wavefield hypercube dramatically reduces the storage requirements for large 3D imaging problems. Minimal artifacts due to the corners of the computational domain do not impair our ability to image the subsurface accurately and are mostly negligible for practical applications. Successful demonstration of the method on LSRTM creates opportunities to accelerate other similar costly techniques, such as elastic anisotropic full waveform inversion (FWI). Our source wavefield reconstruction method applies to media of arbitrary anisotropy and heterogeneity.

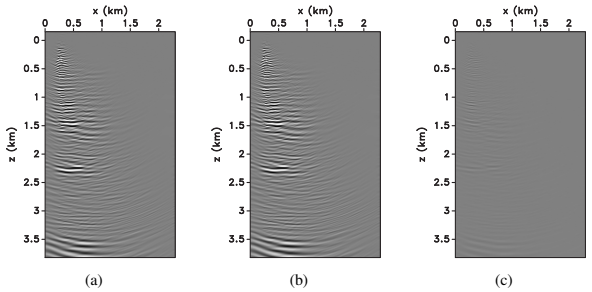

Figure 7: LSRTM image after dip filtering and poststack amplitude gain with one power of depth using (a) reference and (b) reconstructed source wavefields. Panel (c) shows the difference between (a) and (b).

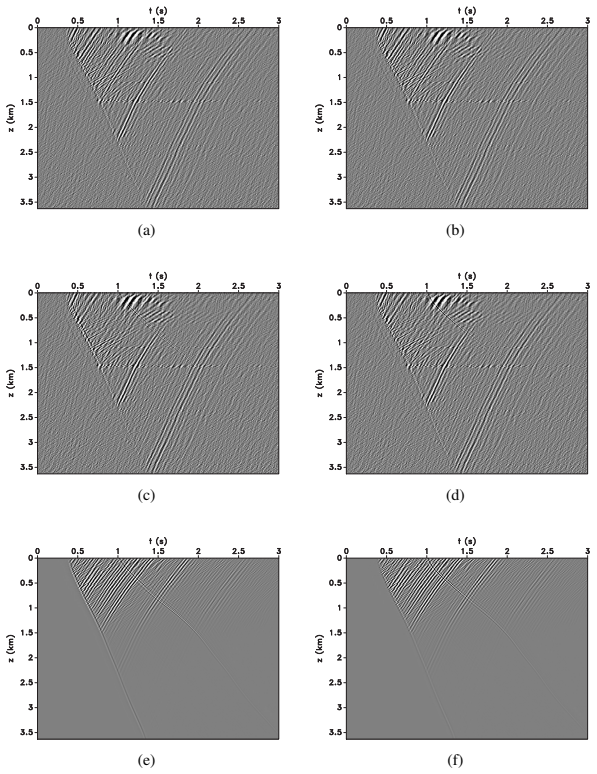

Figure 8: Initial data residuals for single shot LSRTM using (a) reference and (b) reconstructed source wavefields. Panels (c) and (d) show the final data residuals for the corresponding methods. The bottom panels show modeled DAS response using (e) reference and (f) reconstructed source wavefield.

ACKNOWLEDGMENTS

We would like to thank the sponsors of the Center for Wave Phenomena, whose support made this research possible. We thank Whitney Schultz and Jim Simmons of the Reservoir Characterization Program (RCP), Colorado School of Mines for processing the Eagle Ford Shale dataset. We are grateful to Devon Energy Corporation for providing access to the Eagle Ford Shale dataset. The reproducible numeric examples in this paper use the Madagascar open-source software package (Fomel et al., 2013) freely available from http://www.ahay.org.

REFERENCES

Aki, K., and P. G. Richards, 2002, Quantitative seismology, 2nd ed.: University Science Books.

Anderson, J. E., L. Tan, and D. Wang, 2012, Time-reversal checkpointing methods for RTM and FWI: Geophysics, **77**, S93–S103.

Bo, F., and W. Huazhong, 2011, Reverse time migration with source wavefield reconstruction strategy: Journal of Geophysics and Engineering, **9**, 69.

Clapp, R. G., 2009, Reverse time migration with random boundaries: 79th Annual International Meeting, SEG, Expanded Abstracts, 2809–2813.

Dussaud, E., W. W. Symes, P. Williamson, L. Lemaistre, P. Singer, B. Denel, and A. Cherrett, 2008, Computational strategies for reverse-time migration: 78th Annual International Meeting, SEG, Expanded Abstracts, 2267–2271.

Fomel, S., P. Sava, I. Vlad, Y. Liu, and V. Bashkardin, 2013, Madagascar: open-source software project for multidimensional data analysis and reproducible computational experiments: Journal of Open Research Software, **1**.

Gangi, A. F., 1970, A derivation of the seismic representation theorem using seismic reciprocity: Journal of Geophysical Research, **75**, 2088–2095.

Jia, X., and L. Yang, 2017, A memory-efficient staining algorithm in 3D seismic modelling and imaging: Journal of Applied Geophysics, **143**, 62–73.

Liu, S., X. Li, W. Wang, and T. Zhu, 2015, Source wavefield reconstruction using a linear combination of the boundary wavefield in reverse time migration: Geophysics, **80**, S203–S212.

Masson, Y., P. Cupillard, Y. Capdeville, and B. Romanowicz, 2013, On the numerical implementation of time-reversal mirrors for tomographic imaging: Geophysical Journal International, **196**, 1580–1599.

Morse, P. M., and H. Feshbach, 1953, Methods of theoretical physics: McGraw-Hill.

Mulder, W., 2017, Higher-order source-wavefield reconstruction for reverse-time migration from stored values in a boundary strip just one point wide: Geophysics, **83**, 1–27.

Nguyen, B. D., and G. A. McMechan, 2014, Five ways to avoid storing source wavefield snapshots in 2D elastic prestack reverse time migration: Geophysics, **80**, S1–S18.

Raknes, E. B., and W. Weibull, 2016, Efficient 3D elastic full-waveform inversion using wavefield reconstruction methods: Geophysics, **81**, R45–R55.

Ravasi, M., and A. Curtis, 2013, Elastic imaging with exact wavefield extrapolation for application to ocean-bottom 4C seismic data: Geophysics, **78**, S265–S284.

Rocha, D., N. Tanushev, and P. Sava, 2017, Anisotropic elastic wavefield imaging using the energy norm: Geophysics, **82**, S225–S234.

Shen, X., and R. G. Clapp, 2011, Random boundary condition for low-frequency wave propagation: 81st Annual International Meeting, SEG, Expanded Abstracts, 2962–2965.

———, 2015, Random boundary condition for memory-efficient waveform inversion gradient computation: Geophysics, **80**, R351–R359.

Symes, W. W., 2007, Reverse time migration with optimal checkpointing: Geophysics, **72**, SM213–SM221.

Tan, S., and L. Huang, 2014, Reducing the computer memory requirement for 3D reverse-time migration with a boundary-wavefield extrapolation method: Geophysics, **79**, S185–S194.

Vasmel, M., and J. O. Robertsson, 2016, Exact wavefield reconstruction on finite-difference grids with minimal memory requirements: Geophysics, **81**, T303–T309.

Wapenaar, C. P. A., 2014, Elastic wave field extrapolation: Redatuming of single-and multi-component seismic data: Elsevier, **2**.

Yang, P., R. Brossier, and J. Virieux, 2016, Wavefield reconstruction by interpolating significantly decimated boundaries: Geophysics, **81**, T197–T209.

Yang, P., J. Gao, and B. Wang, 2014, RTM using effective boundary saving: A staggered grid GPU implementation: Computers & Geosciences, **68**, 64–72.